

Effect of Ultrasonic Surface Rolling Process on Surface Properties and Microstructure of 6061 Aluminum Alloy

Xiquan Ma^a, Weihai Zhang^b, Shubo Xu^{a,c,*} , Kangwei Sun^a, Xinzhi Hu^a, Guocheng Ren^a,
Jianing Li^a, Xianhua Zhao^d, Fei Gao^d

^aShandong Jianzhu University, School of Materials Science and Engineering, Fengming Road, 1000, Jinan, 250101, Shandong, China.

^bWeifang Fuyuan Supercharger Co, Weifang, 261206, Shandong, China.

^cHuazhong University of Science And Technology, Die & Mould Technology National Key Laboratory, Wuhan, 430074, Hubei, China.

^dShandong Huayun Electromechanical Technology Co, Jinan, 250000, Shandong, China.

Received: July 18, 2023; Revised: September 21, 2023; Accepted: November 08, 2023

Nano-surface layers were prepared on the surface of 6061 aluminum alloy using the ultrasonic surface rolling process (USRP). The surface morphology, surface roughness, microstructure, hardness, and corrosion resistance of 6061 aluminum alloy were systematically characterized using X-ray diffraction (XRD), laser scanning confocal microscopy (LSCM), optical microscope(OM), scanning electron microscopy (SEM), energy dispersive spectrometer (EDS), and other testing methods. The results showed that ultrasonic surface rolling strengthening did not change the surface phase composition of 6061 aluminum alloy. It changed the size of the surface phases and the distance between the phases while refining the surface grains. The static pressures has a great influence on the surface properties of 6061 aluminum alloy. The best surface properties were obtained under 500N static pressures. The surface hardness reached 129.5HV0.5, the surface morphology was flat and continuous, the surface roughness was reduced to Ra0.191 μ m, and the corrosion resistance was significantly improved.

Keywords: USRP, static pressures, 6061 aluminum alloy, Microstructure

1. Introduction

6061 aluminum alloy is an aluminum-magnesium-silicon alloy with excellent processing properties and high toughness^{1,2}, which is widely used in aerospace, transportation, and other fields, and has a crucial position in the field of automotive lightweight. Compared with steel, aluminum alloy has the advantages of being lightweight and high specific strength, but the hardness of aluminum alloy is low, and the surface is easy to be corroded and produce cracks and other defects, and the existence of surface defects further causes fatigue damage, resulting in incalculable losses. Therefore, it is very important to study the surface strengthening of 6061 aluminum alloy to improve the fatigue resistance of 6061 aluminum alloy.

In recent years, surface strengthening techniques such as surface mechanical abrasion treatment(SMAT)³, ultrasonic surface shot peening (USSP)^{4,5}, and surface ultrasonic impact treatment (SUIT)⁶ have been widely used in the field of surface modification of metallic materials. Ultrasonic surface rolling process (USRP), as a surface strengthening technique, can significantly improve surface properties⁷⁻⁹. The principle of USRP is a combination of ultrasonic impact and static rolling, whereby the synergistic effect of high-frequency impact and extrusion results in intense plastic deformation of the surface, thus achieving the purpose of modification¹⁰.

USRP can achieve nanosizing of the surface, i.e., grain size refinement to the nanoscale¹¹, which results in a significant optimization of the surface properties of the material. The principle is shown in Figure 1.

Many alloys have been studied by scholars for performance enhancement after USRP treatment. Tan et al.¹² treated TC17 alloy by USRP and the surface roughness were reduced from 0.5~1.07 μ m to 0.04~0.12 μ m, the friction factor was reduced due to the reduction of roughness, and a dense work-hardened layer was obtained; Ye et al.¹³ treated the specimens by hard turning and ultrasonic tumbling respectively and the surface roughness of the specimens was reduced by 88.5% after treatment, the residual tensile stress was converted into residual compressive stress, the grain size of the specimens was refined, and the properties were significantly improved; Chen et al.¹⁴ investigated the USRP of Mg-Y-Nd-Zr alloy after iso channel angular pressing, the results showed that the surface roughness of Mg alloy was significantly improved after USRP treatment, residual stresses were introduced on the surface of the most superficial layer, and 450 μ m gradient nanostructures were obtained.

Current research on aluminum alloys has focused on the effect of the USRP process on surface properties. Xu et al.¹⁵ investigated the surface integrity and corrosion fatigue properties of 7B50-T7751 aluminum alloy treated with USRP in one, three, and six passes. The results showed

*e-mail: xsb@sdjzu.edu.cn

that a modified surface layer with refined microstructure and increased microhardness was formed after USRP; Sun et al.¹⁶ investigated the effects of different USRP passes on the surface condition, surface organization, and corrosion resistance of this alloy. Ye et al.¹⁷ focused on the effect of the ultrasonic surface rolling process on the surface, properties of QAl10-3-1.5 aluminum bronze alloy under different rolling reductions and rolling times, and the results showed that the surface layer of USRP specimens underwent severe plastic deformation, a significant reduction in surface roughness, the substantial increase in surface hardness, and significant enhancement in wear resistance.

This paper focuses on the USRP process for 6061 aluminum alloy. The surface properties such as surface morphology, surface roughness, surface hardness, etc. under different parameters are investigated by varying different static load force parameters. At the same time, the mechanism of USRP strengthening is investigated by combining the microstructures.

2. Experimental Methods

The test material was a thin sheet of hot-rolled 6061 aluminum alloy and a vertical machining center VMC850B was used to mill a block of size $20 \times 20 \times 10 \text{ mm}^3$ in a sheet of size $100 \times 60 \times 20 \text{ mm}^3$ and to grind the burrs at the edges, as shown in Figure 2. The specific chemical composition of the material is shown in Table 1.

Using the ultrasonic rolling machine Haokeneng HVM1260 performs USRP treatment on the surface of 6061 aluminum alloy, which includes an ultrasonic generation system, a CNC system, and a processing system with a 14 mm diameter WC carbide rolling ball. For the USRP treatment, the ultrasonic power was 28 KHz, the ultrasonic amplitude was $3 \mu\text{m}$, the depth of downward pressure was 0.1 mm, and the step size was 0.1 mm. The static load force was set to 300 N, 500 N, and 700 N as a single variable to obtain the USRP specimens. The untreated specimens are called original pieces (U).

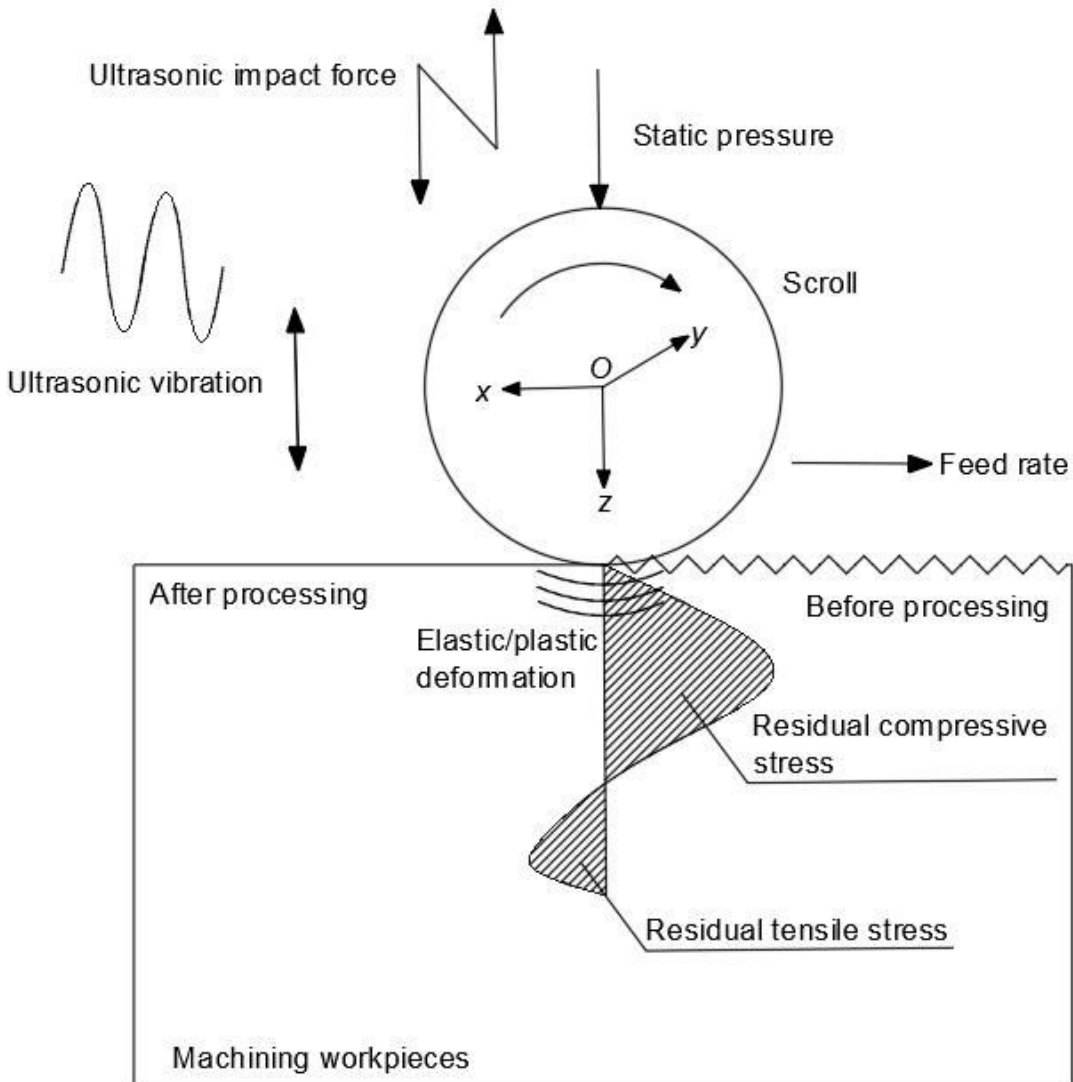


Figure 1. USRP working principle diagram.

The phase structure of the specimens was determined using Cu target XRD. The average grain size of the samples was calculated by the Scherrer-Willson equation¹⁷. Wire Electrical Discharge Machining (WEDM) was used to cut $5 \times 10 \times 10 \text{ mm}^3$ specimens from the USRP-treated specimens for SEM (ZEISS SUPRA55) combined with EDS to observe the surface phase changes. The microhardness of the surface and the gradient microhardness of the cross-section were tested using a Vickers microhardness tester (HVS-1000A). The distance between each indentation is greater than 5 times the width of the indentation to minimize the effect of deformation. The test load was 0.5kg and the holding time was 15s.

The surface morphology before and after USRP treatment was observed and the surface profile height difference and roughness were measured using a laser scanning confocal microscope (LSCM, KC-X1000). The scanning area was $4 \text{ mm} \times 4 \text{ mm}$, the scanning pitch was $5 \mu\text{m}$, and the scanning

speed was $7,500 \mu\text{m/s}$. To reduce the influence of errors, the roughness values of horizontal, vertical, and diagonal lines in the scanning area were measured and averaged as shown in Figure 3.

The electrochemical corrosion performance of the specimens was tested using an electrochemical workstation (Interface1000, China). A $10 \text{ mm} \times 10 \text{ mm}$ sample was used as the working electrode, a platinum sheet as the auxiliary electrode, and a three-electrode system with a glycol-saturated electrode as the reference electrode. The working surface of the specimen was left exposed to corrosion, and all the remaining surfaces were wrapped in epoxy resin. The corrosion medium was 3.5 wt% NaCl solution, and the kinetic potential polarization curve and AC impedance curve were measured at $25^\circ\text{C} \pm 2^\circ\text{C}$. The dynamic potential polarization scan rate was 2 mV/s , and the open circuit potential was $\pm 250 \text{ mV}$; the frequency range of the AC impedance spectrum was $100 \text{ kHz} - 10 \text{ mHz}$, and the AC signal amplitude was 10 mV .

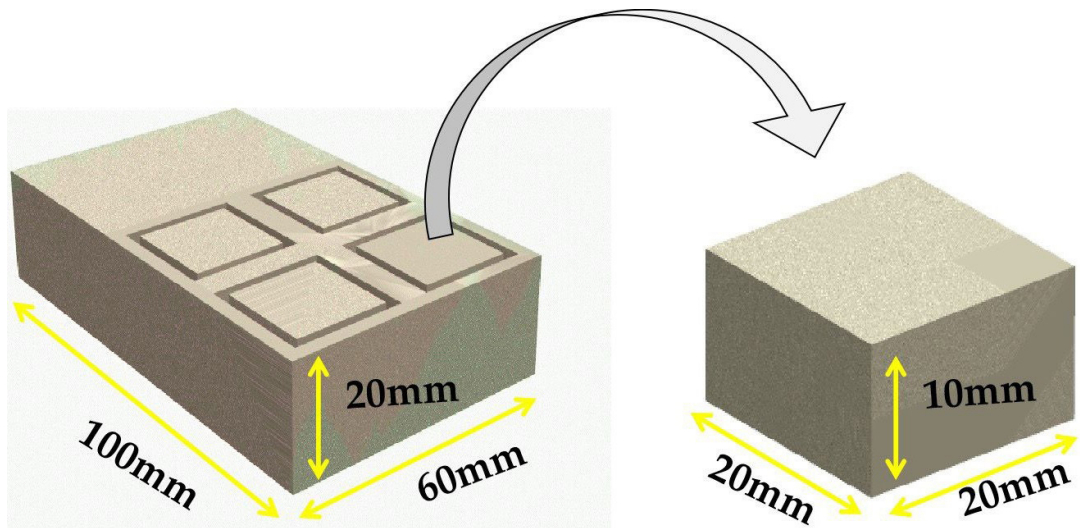


Figure 2. Schematic diagram of specimen size.

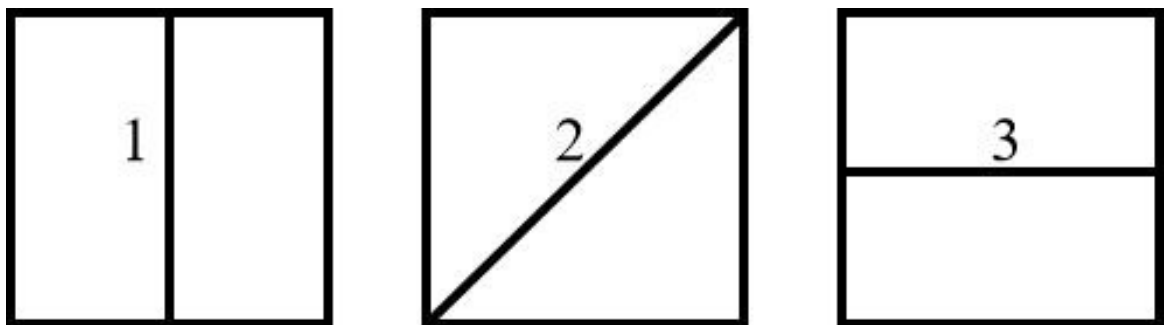


Figure 3. Schematic diagram of surface roughness acquisition Ra1, Ra2 and Ra3.

Table 1. Detailed chemical composition of 6061 aluminium alloy (wt%).

Mg	Si	Fe	Cu	Cr	Mn	Ti	Al
0.816	0.566	0.447	0.203	0.136	0.066	0.035	Bal.

3. Results and Discussion

3.1. XRD analysis

The XRD test results before and after USRP treatment are shown in Figure 4. It can be seen from the figure that the diffraction peaks are in the same position for all specimens, proving that USRP did not change the phase composition of the 6061 aluminum alloy. The FWHM (full width at half maximum) and grain size of the specimens before and after USRP processing are listed in Table 2. The FWHM and crystallite size at 2θ of 38.5° and 44.7° were calculated using Jade5.0 software and the results were averaged for both. The comparison shows that the grain size gradually becomes smaller and the FWHM gradually increases with the increase of static loading force. It can be demonstrated that the surface grain refinement after USRP treatment leads to a larger width of the diffraction peak, and the higher the static loading force applied during USRP treatment, the more pronounced the grain refinement.

3.2. Microstructure analysis

The three-dimensional microstructure of the hot-rolled formed 6061 aluminum alloy sheet has significant differences in the three directions, and its three-dimensional microstructure is shown in Figure 5. The three directions of rolling are RD (rolling direction), TD (transverse direction), and ND (normal direction). The RD-TD surface has a slender fibrous organization; the grains in the ND-TD surface are deformed, and the effect of merit orientation is obvious; the grains in the ND-RD surface are coarser compared with the other two surfaces, and the changes are more obvious after USRP treatment, so in this paper, the microstructure of this face was used as the object of study to explore the microscopic changes after USRP treatment.

During the USRP process, the specimen is subjected to both the impact force in the vertical direction from the rolling head and the shear stress in the rolling direction generated by the rotational motion, which results in severe plastic deformation and refinement of the grains. And the shear stress in the rolling direction is generated by the rotational motion, which results in severe plastic deformation and refinement of the grains.

The cross-sectional microstructure of the specimens under different static pressures is shown in Figure 6. After the USRP treatment, a distinct gradient strengthening layer was formed in the surface layer of the cross-section. Here the gradient strengthening layer was divided into the refinement zone and transition zone. The results show that with the increase of static loading force, the size of the refinement zone and transition zone gradually increases, the grains are elongated and the grain refinement is more obvious; the size difference

between the gradient strengthening layer at 500N and 700N is not large, which means that when the static loading force reaches 500N, the effect of USRP gradient strengthening is close to a critical value, and the static loading force does not play a major role in the strengthening effect of the surface at this time. Since the aluminum alloy is a face-centered cubic (fcc) structure, it has 12 slip systems, which are subjected to multi-system slip and relative slip mechanisms, resulting in plastic deformation¹⁸. Therefore, the greater the static load force at USRP, the greater the shear stress effect, so the greater the degree of deformation and the greater the depth of the reinforced layer.

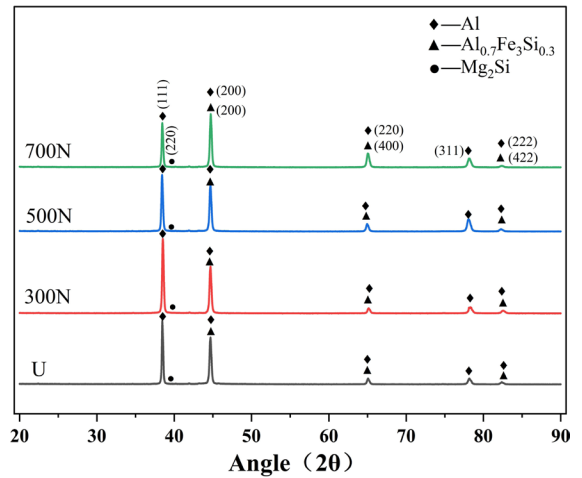


Figure 4. XRD patterns of specimens under different static pressures.

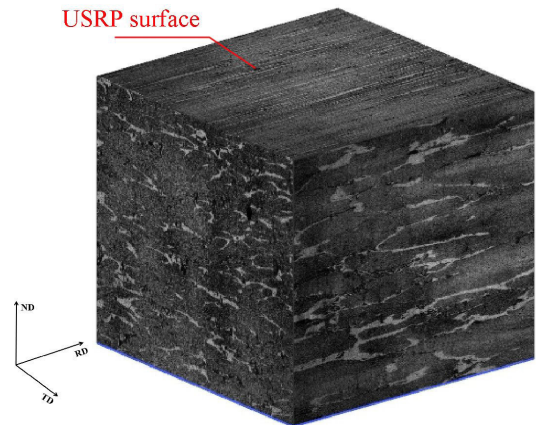


Figure 5. Three-dimensional microstructure (OM) of hot-rolled 6061 aluminum alloy.

Table 2. Calculated data of specimens under different static pressures.

static pressures	FWHM	Average crystallite size(nm)
U	0.281	—
300N	0.331	299
500N	0.359	273
700N	0.373	262

The SEM combined with EDS analysis of the specimen surface before and after USRP treatment is shown in Figure 7. The AlFeSi phase in the specimen without USRP treatment is present in bone and needle shape; after USRP treatment, AlFeSi is refined, and present in interrupted shape at the grain boundaries. From the corresponding EDS energy spectrum

analysis, it is clear that O and Cu appear in the AlFeSi phase after USRP treatment. It is speculated that O and Cu may be present in the second phase in the form of CuO, which improves electron conduction and makes the passivation film more dense, thus slowing down the corrosion process and improving corrosion resistance¹⁹.

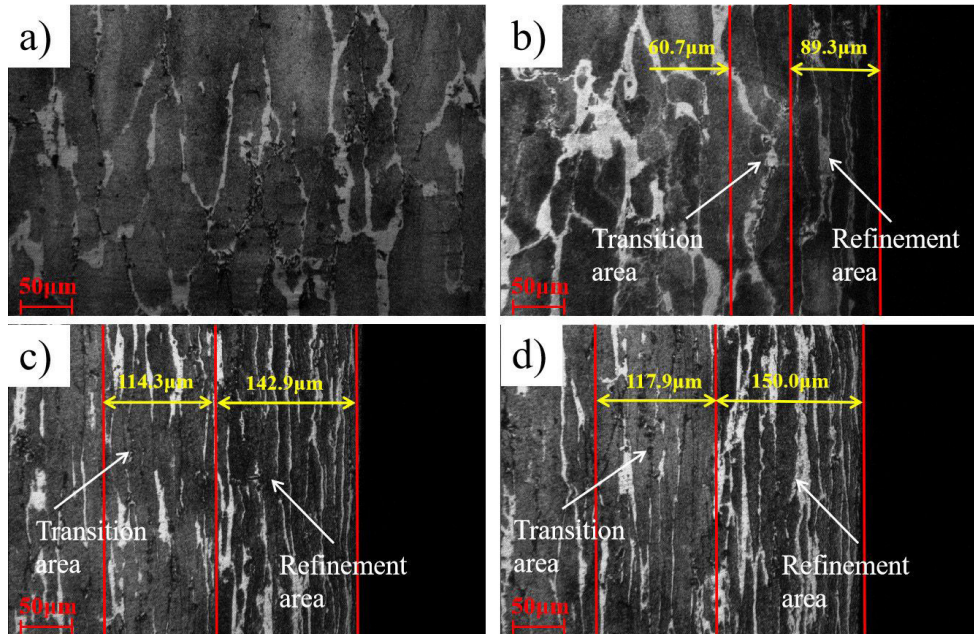


Figure 6. Cross-sectional microstructures(OM) of specimens under different static pressures: (a) original specimen; (b) 300N; (c) 500N; (d) 700N.

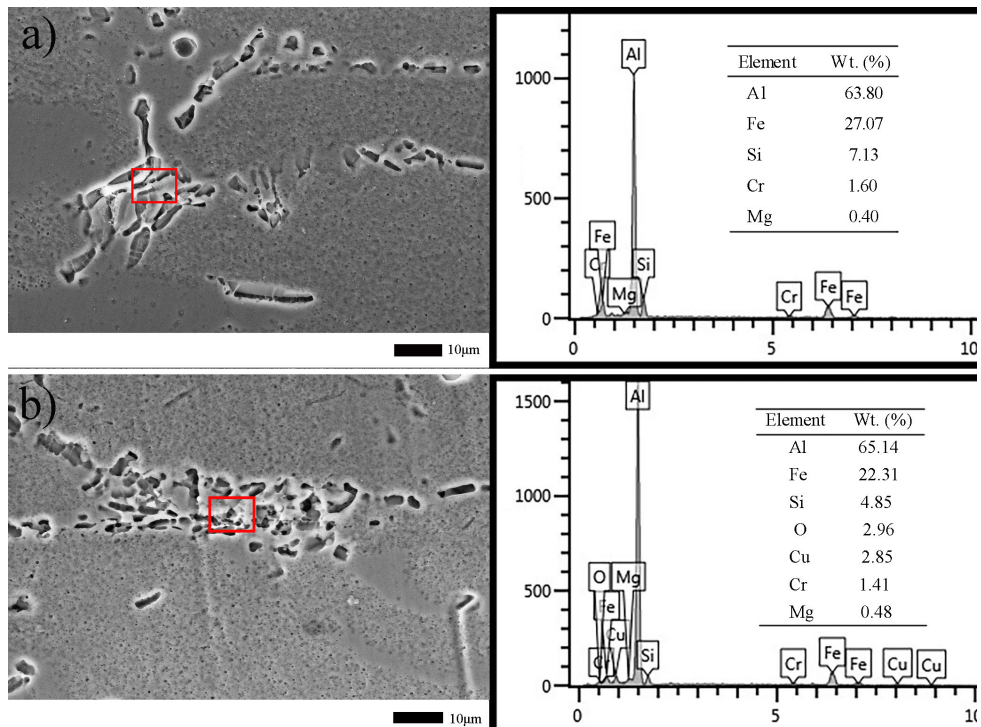


Figure 7. Changes in surface AlFeSi phase of 6061 aluminum alloy before and after USRP(SEM): (a) Before USRP; (b) After USRP.

The AlFeSi phase on the surface of the USRP-treated specimens under different static pressures was further analyzed. The SEM images of the AlFeSi phase on the specimen surface are shown in Figure 8. The results show that the size of the AlFeSi phase gradually becomes smaller and the distance between phases gradually becomes larger with the increase of static loading force. During the USRP treatment, the increase of static loading force makes the plastic deformation of the specimen surface more intense so that the surface grains are refined while the AlFeSi phase is refined as well. The smaller the size of the AlFeSi phase and the larger the spacing between the AlFeSi phase and phase, the smaller the surrounding aluminum substrate is corroded²⁰. Therefore, from the effect of the AlFeSi phase in the local corrosion of 6061 aluminum alloy, the greater the static loading force at USRP, the smaller the scope of corrosion influence of the AlFeSi phase on its surrounding aluminum substrate, and the better its corrosion resistance.

3.3 Hardness analysis

The surface hardness of the specimens after USRP treatment with different static pressures is shown in Figure 9.

Figure 9a shows the surface hardness of the original specimen was only 97.2 HV_{0.5}, when the static load force was 300 N, the surface hardness was 116.93 HV_{0.5}, which increased by 20.3%; when the static load force was 500 N, the surface hardness was 129.6 HV_{0.5}, which increased by 33.3% compared with the original specimen. The hardness increases with the increase of static load force. When the static load force is 700 N, the hardness decreases compared to 500 N. At this point, the static load force plays a secondary role in the hardness increase. The reason for this is that hardness mainly follows the Hall-Petch relationship²¹. When the static loading force is greater than 500 N, the hardness remains essentially constant because the grain size of the specimen does not change significantly. The variation of the cross-sectional microhardness of the specimen with depth is shown in Figure 9b. It can be seen that the hardness tends to decrease gradually with the increase in depth, and the trend of change is more or less the same between different static pressures. Further analysis shows that the greater the static load force, the greater the deformation of the specimen, the more obvious the process hardening phenomenon, and therefore the greater the hardness.

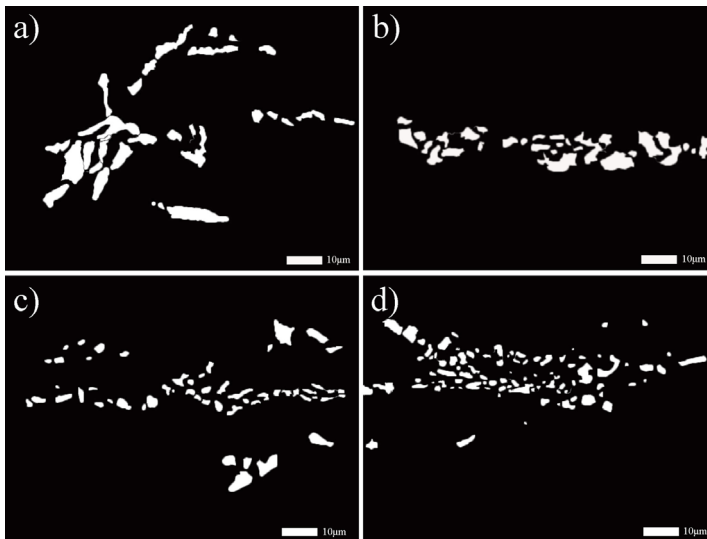


Figure 8. SEM of AlFeSi phase on specimen surface under different static pressures: (a) original specimen; (b)300N;(c)500N;(d)700N.

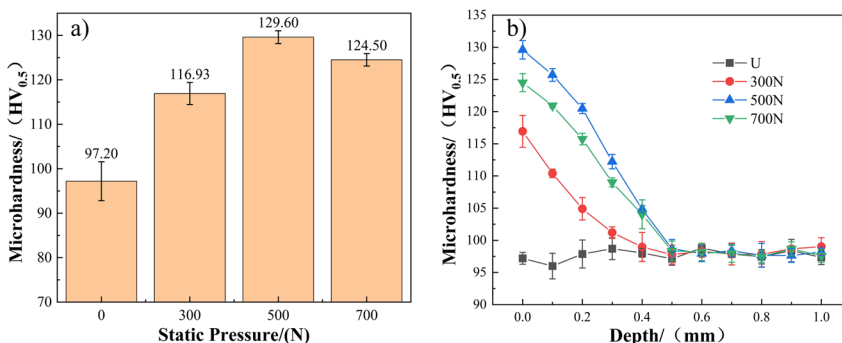


Figure 9. Microhardness of specimens under different static pressures: a) surface microhardness; b) gradient microhardness of the cross-section along the depth direction.

3.4. Surface morphology and surface roughness

The surface morphology before and after USRP treatment under different static pressures is shown in Figure 10a shows the sample without USRP treatment, and its surface is uneven; Figure 10b shows the sample surface becomes flat and smooth after USRP treatment under 300N static load force, forming a uniform and continuous plane, and the surface bump disappears; (c) and (d) show the surface morphology after USRP treatment under 500N and 700N, respectively, and both have obvious USRP traces, and at 700N, the surface appears (e), (f), (g), and (h) corresponds to the surface profile height changes in (a), (b), (c), and (d), respectively. The surface profile height fluctuations were large before the USRP treatment and became significantly smaller after the USRP treatment. The maximum height, minimum height, and height difference of the surface profile after USRP treatment with different static load forces are shown in Table 3. It was found that the height difference of the surface contour of the USRP-treated specimens was significantly reduced, and the lowest height difference of the surface contour was 9.8 μm at a static load force of 500 N. It was proved that USRP could make the surface flat and the effect of cutting the peaks and filling the valleys was obvious²².

The surface roughness before and after USRP treatment under different static load forces is shown in Figure 11. The trend of the surface roughness values under different

static pressures is the same, the higher the static loading force, the smaller the surface roughness value. When the static load force reaches 500N, the surface roughness is the smallest at Ra0.191 μm , which is about 10 times lower than that of the original specimen Ra1.773 μm ; when the static load force reaches 700N, the roughness value increases slightly compared with that at 500N, which is due to the reduction of roughness caused by the generation of fine crack defects on the surface, echoing the study of surface profile in the previous paper. All three sets of roughness values corresponding to each static load force have the smallest value of Ra₃ and the largest value of Ra₁. Ra₃ is the roughness value along the machining direction and Ra₁ is the roughness value in the vertical machining direction. Therefore, it can be inferred that the roughness value along the machining direction is smaller than the roughness value perpendicular to the machining direction. Therefore, in this paper, the average value of roughness in three directions is used as the surface roughness. The semi-empirical formula for calculating the surface stress concentration coefficient using surface roughness parameters is expressed by Equation 1²³:

$$K_t = 1 + n \sqrt{\lambda \frac{R_z}{\rho}} \quad (1)$$

where K_t is the stress concentration factor, λ is the ratio of profile spacing to depth, and ρ is the effective radius of curvature of the profile valley.

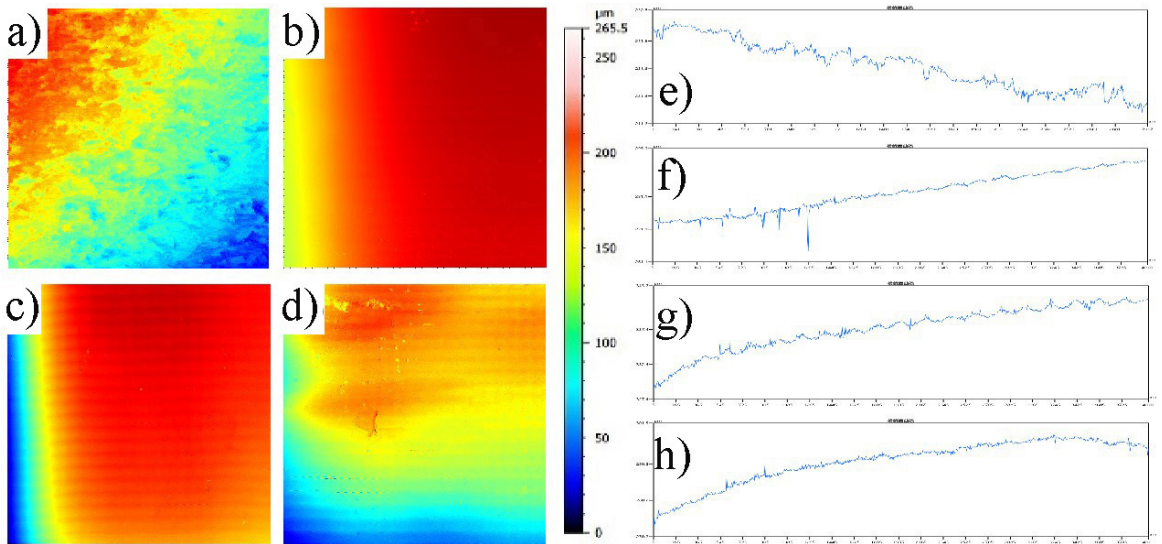


Figure 10. Surface morphology and surface profile height of specimens under different static pressures: a) and e) original specimen; b) and f) 300N; c) and g) 500N; d) and h) 700N.

Table 3. Difference in surface profile height of specimens under different static pressures.

static pressures	Max altitude	Min altitude	Altitude intercept
U	248.6 μm	213.5 μm	35.1 μm
300N	287.3 μm	274.2 μm	13.1 μm
500N	339.5 μm	329.7 μm	9.8 μm
700N	294.2 μm	276.5 μm	17.7 μm

This equation can be used to explain the effect of surface roughness on fatigue resistance performance. Fatigue cracks usually originate on surfaces where there are small peaks and valleys, such as scratches and cracks, which can cause stress concentrations. The presence of stress concentrations reduces the fatigue strength of the part²⁴. Therefore, the quality of the surface has a great impact on the life of the part. The smoother the surface, the more difficult it is to sprout fatigue cracks. The semi-empirical formula for calculating the surface stress concentration factor from the surface roughness parameter shows that USRP reduces the surface roughness, which is less likely to form stress concentrations and improves the fatigue resistance of the material.

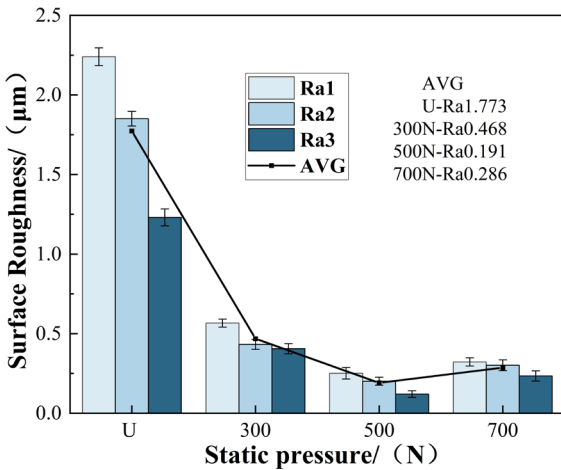


Figure 11. Surface roughness of specimens under different static pressures.

3.5. Electrochemical corrosion analysis

Figure 12a shows the dynamic polarization curves of the USRP-treated specimens under different static pressures. As can be seen from Figure 12a, the higher the static loading force, the higher the self-corrosion potential (E_{corr}) shifts to the right and a very obvious passivation zone appears in the anodic region, indicating that a dense passivation film is formed on the surface of the USRP-treated specimen. However, if the static loading force is too high, cracks will appear in the passivation film and the protection capacity will be reduced, thus decreasing the corrosion resistance of the surface. The values of E_{corr} , I_{corr} , anodic polarization rate (β_a), and cathodic polarization rate (β_c) are listed in Table 4. The results show that the I_{corr} at a static loading force of 500 N is one order of magnitude lower compared to the unprocessed specimen. As the static loading force increases, the I_{corr} gradually decreases. When the static load force increases to 700 N, the I_{corr} increases slightly compared to that at 500 N.

Figure 12b illustrates the Nyquist plots of USRP-treated specimens under different static pressures. Figure 12c shows the variation of polarization resistance R_p with static load force obtained by fitting the EIS curve. Since the radius of the capacitive arc is correlated with the electrochemical transfer resistance²⁵. As can be seen from Figure 12b, the curves of 6061 aluminum alloy specimens under different static loads all show semicircular arcs, which are typical capacitive arcs, indicating that the whole electrode process is controlled by electrochemical reactions. The diameter of the capacitive arc reflects the difficulty of charge transfer on the surface of the specimen. Figure 12b and Figure 12c together illustrate that the USRP-treated specimens have better corrosion resistance.

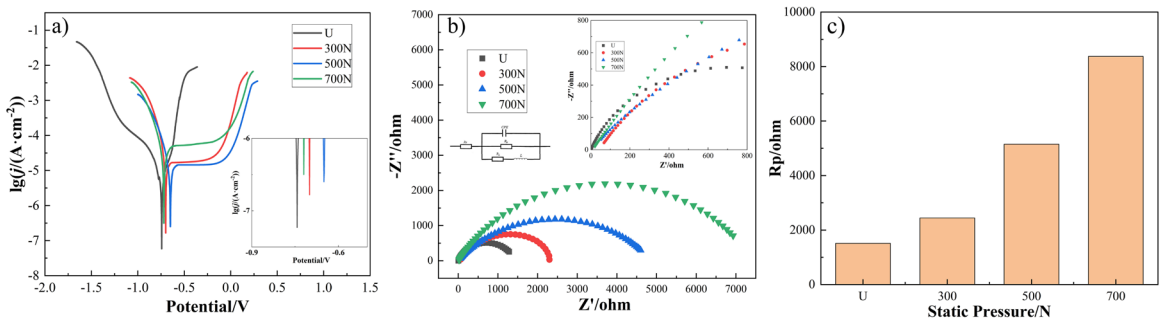


Figure 12. Electrochemical corrosion data under different static pressures: (a) OCP curve and (b) Nyquist diagram (c) Variation of R_p with static load force in 3.5% NaCl solution

Table 4. Parameters of dynamic polarization curves of USRP specimens under different static pressures.

Static pressures	β_a	β_c	E_{corr}	i_{corr}
	(mV/Dec-1)	(mV/Dec-1)	(mV)	(μAcm^{-2})
U	8.13	-3.492	-743	61.7
300N	3.07	-12.468	-701	17.8
500N	2.732	-9.679	-652	9.3
700N	4.051	-10.121	-720	22.4

As the static loading force increases, the diameter of the capacitive resistance arc increases, indicating that the charge transfer on the surface of the specimen is progressively more difficult, the electrochemical transfer resistance increases, and the passivation film formed on the surface of the specimen is more stable with better corrosion performance. When the static load force reaches 700N, the capacitive arc diameter reaches the maximum value, about 4.5 times of the unprocessed specimen.

In this study, we mainly start with the static load force to investigate the effect of USRP on the surface hardness, surface roughness, corrosion resistance, and microstructure of 6061 aluminum alloy in order to reveal the fatigue-strengthening mechanism of 6061 aluminum alloy. We believe that the effect of residual stress on the fatigue properties of 6061 aluminum alloy can be studied subsequently. Residual compressive stress can effectively inhibit surface crack initiation and extension²⁶, and USRP can preset higher residual compressive stress on the material surface. Alternatively, we can conduct a more in-depth study on the effects of the number of USRP on the microstructure and fatigue properties of 6061 aluminum alloy²⁷.

4. Conclusion

In this paper, the effects of different static pressures on the surface properties and microstructure of 6061 aluminum alloy were investigated by changing the static loading force during USRP treatment. And the conclusion can be shown:

- (1). USRP does not change the phase composition of 6061 aluminum alloy, but after USRP treatment, the grains and AlFeSi phase are refined. the AlFeSi phase becomes intermittent at the grain boundaries from the original bone-like or needle-like. With the increase of static loading force, the size of the AlFeSi phase gradually decreases and the distance between phases gradually increases, so the smaller the range of corrosion influence of AlFeSi relative to its surrounding aluminum substrate, the better its corrosion resistance.
- (2). With the increase of static load force, the surface hardness of 6061 aluminum alloy gradually increases, reaching the maximum of 129.6HV_{0.5} at 500N, compared with the original specimen increased by 33.3%, the hardness slightly decreases at 700N, at this time the static load force plays a secondary role in the increase of hardness. decreases with depth.
- (3). After USRP treatment, the surface shape of 6061 aluminum alloy becomes flat, and the effect of cutting peaks and filling valleys is obvious, the surface is the flattest at 500N, the height difference of the surface profile is the smallest, 9.8μm; the surface roughness is also the smallest, Ra0.191μm.
- (4). The USRP treatment forms a dense passivation film on the surface of 6061 aluminum alloy, and the corrosion resistance is significantly improved. The improvement of corrosion resistance is mainly related to the synergistic effect of surface grain refinement and reduction of surface roughness.

5. Acknowledgment

This work was supported by the Natural Science Foundation of Shandong Province under grant no. ZR2021ME182, the National Natural Science Foundation of China under grant no. 52001187, the Shandong Province New Old Energy Conversion Major Project (New Energy Industry 2021-03-3) and the Science and Technology Enterprise Innovation Program of Shandong Province, China (2022TSGC2108, 2022TSGC2402, 2023TSGC085, 2023TSGC0119, 2023TSGC0759 and 2023TSGC0961).

6. Reference

1. Kolobnev N, Ber L, Khokhlatova L, Ryabov DK. Structure, properties, and application of alloys of the Al–Mg–Si–(Cu) system. *Metal Sci Heat Treat.* 2012;53(9-10):440-4. <http://dx.doi.org/10.1007/s11041-012-9412-8>.
2. Cui L, Guo MX, Peng X, Zhang Y, Zhang J, Zhuang L. Influence of pre-deformation on the precipitation behaviors of Al-Mg-Si-Cu alloy for automotive application. *Acta Metall Sin.* 2015;51(3):289-97. <http://dx.doi.org/10.11900/0412.1961.2014.00348>.
3. Azadmanjiri J, Berndt CC, Kapoor A, Wen C. Development of surface nano-crystallization in alloys by Surface Mechanical Attrition Treatment (SMAT). *Crit Rev Solid State Mater Sci.* 2015;40(3):164-81. <http://dx.doi.org/10.1080/10408436.2014.978446>.
4. Chen H, Guan Y, Zhu L, Li Y, Zhai J, Lin J. Effects of ultrasonic shot peening process parameters on nanocrystalline and mechanical properties of pure copper surface. *Mater Chem Phys.* 2021;259:124025. <http://dx.doi.org/10.1016/j.matchemphys.2020.124025>.
5. Zhu S, Hu Y, Zhang X, Zou Y, Ahmad T, Zhang W, et al. Experimental investigation on ultrasonic shot peening of WC-Co alloy. *Mater Manuf Process.* 2020;35(14):1576-83. <http://dx.doi.org/10.1080/10426914.2020.1779943>.
6. Zhou C, Wang J, Guo C, Zhao C, Jiang G, Dong T, et al. Numerical study of the ultrasonic impact on additive manufactured parts. *Int J Mech Sci.* 2021;197:106334. <http://dx.doi.org/10.1016/j.ijmecsci.2021.106334>.
7. Qin T, Ao N, Ren X, Zhao X, Wu S. Determination of optimal ultrasonic surface rolling parameters to enhance the fatigue strength of railway axle EA4T steel. *Eng Fract Mech.* 2022;275:108831. <http://dx.doi.org/10.1016/j.engfracmech.2022.108831>.
8. Liu Z, Zhao H, Zhang C, He Z, Ji V. Investigation on the evolution of residual stress in ultrasonic surface rolling treatment-processed 18CrNiMo7-6 alloy steel. *Trans Indian Inst Met.* 2023;76(3):777-85. <http://dx.doi.org/10.1007/s12666-022-02776-2>.
9. Ren S, Zhang Y, Zhao Y, An Z, Xue F, Yao J, et al. Enhanced surface properties and microstructure evolution of Cr12MoV using ultrasonic surface rolling process combined with deep cryogenic treatment. *J Mater Eng Perform.* 2019;28(2):1132-40. <http://dx.doi.org/10.1007/s11665-018-3843-3>.
10. Liu Y, Zhao X, Wang D. Determination of the plastic properties of materials treated by ultrasonic surface rolling process through instrumented indentation. *Mater Sci Eng A.* 2014;600:21-31. <http://dx.doi.org/10.1016/j.msea.2014.01.096>.
11. Ye H, Sun X, Liu Y, Rao X, Gu Q. Effect of ultrasonic surface rolling process on mechanical properties and corrosion resistance of AZ31B Mg alloy. *Surf Coat Tech.* 2019;372:288-98. <http://dx.doi.org/10.1016/j.surfcoat.2019.05.035>.
12. Tan L, Yao C, Zhang D, Ren J, Shen X, Zhou Z. Effects of different mechanical surface treatments on surface integrity of TC17 alloys. *Surf Coat Tech.* 2020;398:126073. <http://dx.doi.org/10.1016/j.surfcoat.2020.126073>.

13. Ye H, Zhu J, Liu Y, Liu W, Wang D. Microstructure and mechanical properties of laser clad CrNi alloy by hard turning (HT) and ultrasonic surface rolling (USR). *Surf Coat Tech.* 2020;393:125806. <http://dx.doi.org/10.1016/j.surfcoat.2020.125806>.
14. Chen L, Li W, Sun Y, Luo M. Effect of microstructure evolution on the mechanical properties of a Mg–Y–Nd–Zr alloy with a gradient nanostructure produced via ultrasonic surface rolling processing. *J Alloys Compd.* 2022;923:166495. <http://dx.doi.org/10.1016/j.jallcom.2022.166495>.
15. Xu X, Liu D, Zhang X, Liu C, Liu D, Zhang W. Influence of ultrasonic rolling on surface integrity and corrosion fatigue behavior of 7B50-T7751 aluminum alloy. *Int J Fatigue.* 2019;125:237-48. <http://dx.doi.org/10.1016/j.ijfatigue.2019.04.005>.
16. Sun Q, Yang M, Jiang Y, Lei L, Zhang Y. Achieving excellent corrosion resistance properties of 7075 Al alloy via ultrasonic surface rolling treatment. *J Alloys Compd.* 2022;911:165009. <http://dx.doi.org/10.1016/j.jallcom.2022.165009>.
17. Ye H, Chen A, Liu S, Zhang C, Gao Y, Li Q, et al. Effect of ultrasonic surface rolling process on the surface properties of QA110-3-1.5 aluminum bronze alloy. *Surf Coat Tech.* 2022;433:128126. <http://dx.doi.org/10.1016/j.surfcoat.2022.128126>.
18. Ting W, Dongpo W, Gang L, Baoming G, Ningxia S. Investigations on the nanocrystallization of 40Cr using ultrasonic surface rolling processing. *Appl Surf Sci.* 2008;255(5):1824-9. <http://dx.doi.org/10.1016/j.apsusc.2008.06.034>.
19. Li X, Wang X, Chen B, Gao M, Jiang C, Yuan H, et al. Effect of ultrasonic surface rolling process on the surface properties of CuCr alloy. *Vacuum.* 2023;209:111819. <http://dx.doi.org/10.1016/j.vacuum.2023.111819>.
20. He T, Shi W, Xiang S, Huang C, Ballinger RG. Influence of aging on corrosion behaviour of the 6061 cast aluminium alloy. *Materials.* 2021;14(8):1821. <http://dx.doi.org/10.3390/ma14081821>.
21. Zhang S, Wang F, Huang P. Enhanced Hall-Petch strengthening in graphene/Cu nanocomposites. *J Mater Sci Technol.* 2021;87:176-83. <http://dx.doi.org/10.1016/j.jmst.2021.02.013>.
22. Huang P, Wang Y, Lin J, Cheng Y, Liu F, Qiu Q. Effect of ultrasonic rolling on surface integrity, machining accuracy, and tribological performance of bearing steels under different process schemes. *CIRP J Manuf Sci Technol.* 2023;43:143-57. <http://dx.doi.org/10.1016/j.cirpj.2023.03.003>.
23. Arola D, Williams CL. Estimating the fatigue stress concentration factor of machined surfaces. *Int J Fatigue.* 2002;24(9):923-30. [http://dx.doi.org/10.1016/S0142-1123\(02\)00012-9](http://dx.doi.org/10.1016/S0142-1123(02)00012-9).
24. Sinaiskii BN. Effect of stress concentration on the fatigue resistance of creep-resisting nickel alloys in asymmetric multicycle loading. Report 1. *Strength Mater.* 1984;16(3):372-8. <http://dx.doi.org/10.1007/BF01530031>.
25. Hirschorn B, Orazem ME, Tribollet B, Vivier V, Frateur I, Musiani M. Constant-phase-element behavior caused by resistivity distributions in films: II. Applications. *J Electrochem Soc.* 2010;157(12):C458. <http://dx.doi.org/10.1149/1.3499565>.
26. Wu D, Lv H, Wang H, Yu J. Surface micro-morphology and residual stress formation mechanisms of near-net-shaped blade produced by low-plasticity ultrasonic rolling strengthening process. *Mater Des.* 2022;215:110513. <http://dx.doi.org/10.1016/j.matdes.2022.110513>.
27. Lan S, Qi M, Zhu Y, Liu M, Bie W. Ultrasonic rolling strengthening effect on the bending fatigue behavior of 12Cr2Ni4A steel gears. *Eng Fract Mech.* 2023;279:109024. <http://dx.doi.org/10.1016/j.engfracmech.2022.109024>.